Bulletin of the Seismological Society of America, Vol. 76, No. 1, pp. 19–42, February 1986

SOURCE SPECTRA OF GREAT EARTHQUAKES: TELESEISMIC CONSTRAINTS ON RUPTURE PROCESS AND STRONG MOTION

BY HEIDI HOUSTON AND HIROO KANAMORI

ABSTRACT

Short-period body waves recorded at teleseismic distances from great earthquakes provide information about source rupture processes and strong motions. First, we examine mostly WWSSN records of 19 earthquakes of moment magnitude M_w of 6.5 to 9.5. Four parameters are measured from the short-period *P*-wave train: the maximum amplitude; the period at maximum amplitude; the time between the first arrival and when the maximum amplitude is attained; and coda length. An extension, $\hat{m}_b$, of the teleseismic magnitude, m_b, is defined using the maximum amplitude of the entire short-period *P*-wave rather than the amplitude achieved in the first few *P*-wave cycles. A least-squares fit to the data yields the following relationship between $\hat{m}_b$ and M_w: $m_b = 0.53\ M_w + 2.70$ for M_w 6.5 to 9.5. The time from the first arrival until the maximum amplitude is achieved and the coda length are roughly proportional to M_w, but are further interpreted by a simple asperity model of the rupture process. These data support that short-period waves are, on average, generated preferentially in the same regions of the fault plane as long-period waves (with periods of 10 to 50 sec).

We analyze the spectra of short- and intermediate-period teleseismic GDSN records for seven earthquakes with M_w's of 6.4 to 7.8 and hand-digitized short-period WWSSN records of the 1971 San Fernando earthquake. Significant differences exist between the spectra of different events, due partly to variations in tectonic setting or seismic coupling. Using the digital data, we also investigate the relationship between time-domain amplitude and spectral amplitude for short-period *P* waves. From our empirical relation between spectral amplitude and time-domain amplitude, we estimate the spectral amplitudes implied by the $\hat{m}_b$ data. We compare our results to the ω^{-2} and Gusev spectral models. Neither model can completely represent the data. Nevertheless, we consider the ω^{-2} model a useful reference model for comparing different events. The average source spectrum of six large events with M_w 7.4 to 7.8 does not have the spectral structure suggested by Gusev.

An application to strong motion modeling is presented in which a 1971 San Fernando teleseismic short-period record is summed up to simulate teleseismic records produced by five great earthquakes. The summation procedure matches the moment of the event to be simulated, and includes rupture propagation, fault plane roughness, and randomness. The $\hat{m}_b$ data provide an important constraint on the summation procedures. Thus constrained, this summation procedure can be more confidently used with near-field strong motion records as Green's functions to predict strong motions from great earthquakes.

INTRODUCTION

Although the earthquake source spectrum is commonly characterized well at long periods by seismic moment, it is poorly determined at shorter periods. In this paper, we will be concerned with periods of 1 to 10 sec and will refer to these as short periods, although strong motions with periods of 1 to 10 sec are commonly called long-period strong motions. The source spectrum at short periods has implications for the earthquake rupture process and for strong motions. For example, knowledge of the earthquake source spectrum at periods of 1 to 10 sec is important for the safe

engineering design of large structures such as high-rise buildings or oil drilling platforms near fault zones, particularly near subduction zones.

Strong ground motions from great earthquakes have not been recorded reliably due to the infrequent occurrence of great earthquakes and the large amplitudes generated by great earthquakes, which saturate most nearby seismometers. Therefore, the nature of the source spectrum of great earthquakes is poorly known at present. However, short-period waves from great earthquakes have been recorded at teleseismic distances. Figure 1 shows short-period records of some great earthquakes from the World Wide Standardized Seismographic Network (WWSSN). Because these waveforms are so complex, it is impossible to analyze them deterministically, but the overall character of the waveform can provide useful information on the nature of the seismic source. Despite the importance of short-period radiation, only a few studies have been made on these teleseismic records due to their complexity (Koyama and Zheng, 1983, 1985; Houston and Kanamori, 1983; Purcaru, 1984).

The WWSSN has operated since the early 1960's and has recorded seven earthquakes with moment magnitudes greater than 8.0. In the past few years, high-quality digital records have become available from the Global Digital Seismic Network (GDSN). In this paper, we present a new data set characterizing great earthquakes at short periods. First, we examine WWSSN records of 18 earthquakes of magnitude 6.5 to 9.2 and various short-period records for the 1960 Chilean event of magnitude 9.5. We define a magnitude, $\hat{m}_b$, which is determined at teleseismic distances but is analogous to local magnitude, M_L, determined at short distances. Four parameters are measured from the short-period P-wave train: the maximum amplitude; the period at maximum amplitude; the time between the first arrival and when the maximum amplitude is attained; and coda length. Our parameterization of the overall character of the waveform is interpreted in terms of a simple asperity model of the rupture process. Then we analyze GDSN records for seven earthquakes of magnitude 6.4 to 7.8. The digital data are Fourier-transformed. The resulting displacement spectra are corrected for instrument response, attenuation, geometrical spreading, and radiation pattern, and then averaged to determine source spectra from 1 to 20 sec. Using digitally recorded or hand-digitized records, we also estimate the relationship between time-domain amplitude and spectral amplitude empirically for short-period P waves. This enables us to estimate spectral amplitudes from $\hat{m}_b$. Combining those spectral amplitudes with the directly determined spectra, we determine source spectra for earthquakes with M_w = 6.4 to 9.5. Finally, we discuss the implications of these data for source spectral models and for predictions of strong motions.

WWSSN Data

For all but one of the 19 events studied, we examined 8 to 27 records from WWSSN short-period vertical seismometers at teleseismic distances of 30° to 100°. For the 1960 Chilean event, various short-period records were used, including records written by Benioff short-period, Wood-Anderson, Willmore short-period, and Milne-Shaw seismometers. More than 330 records were studied.

We measured A, the maximum amplitude seen in the P-wave train, and T, the period at the maximum amplitude. An extension, $\hat{m}_b$, of the teleseismic magnitude, m_b, is defined using the maximum amplitude of the entire short-period P wave

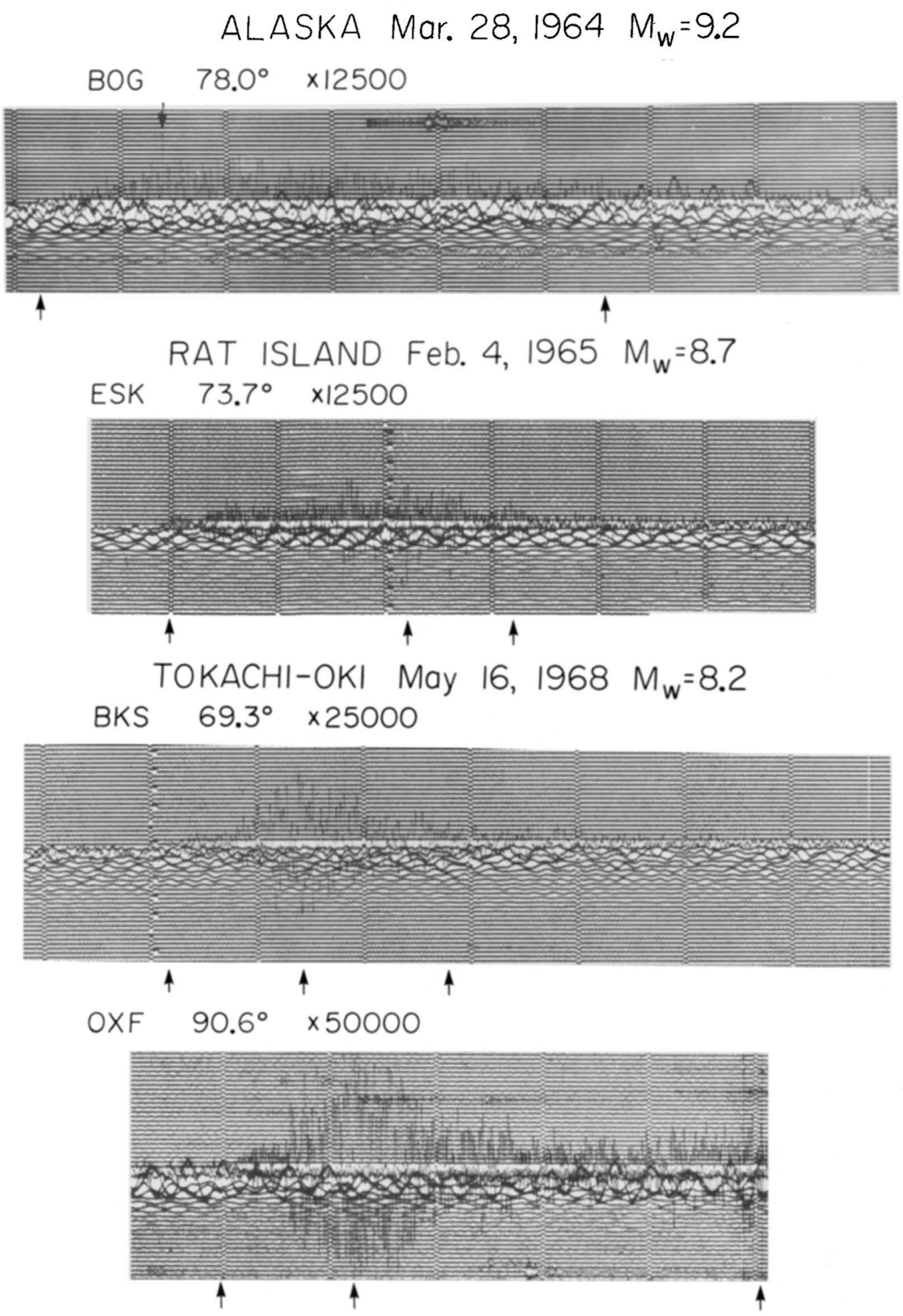

FIG. 1. Teleseismic short-period vertical records of three great earthquakes recorded by WWSSN. Note the minute marks. Arrows show the beginning of the *P* wave, the time the maximum amplitude is achieved, and the coda length as defined in the text.

rather than the maximum amplitude achieved in the first few P-wave cycles

$$\hat{m}_b = \log \frac{A_g}{T} + Q(\Delta) \tag{1}$$

where A_g is the true amplitude of the maximum ground displacement obtained from A and the instrument gain at T, and $Q(\Delta)$ is the empirical Gutenberg-Richter distance calibration function for PZ waves (or PH waves for Wood-Anderson records of the 1960 Chilean event). The period at the maximum amplitude, T, enters (1) explicitly, and implicitly through A_g because the gain depends strongly on T. Koyama and Zheng (1985) measured an average period of several cycles around the maximum amplitude (Koyama, personal communication, 1985). The range of T

TABLE 1

SUMMARY OF RESULTS

Event ID	No. of Stations	T (sec)	C (min)	T_M (min)	$\hat{m}_b$	M_w	M_S
0 Chile 1960	13	2.19	5.74	2.44	7.57	9.5	8.5
1 Alaska 1964	19	1.81	5.63	1.43	7.64	9.2	8.4
2 Rat Island 1965*	17	1.48	5.08	0.77	7.19	8.7	8.2
				2.31			
3 Kurile Island 1963	20	1.73	3.30	1.49	7.23	8.5	8.1
4 Sumbawa 1977	8	1.89	4.44	0.82	7.47	8.3	8.1
5 Tokachi-Oki 1968	27	1.56	3.96	1.35	7.18	8.2	8.1
6 Kurile Island 1969	9	1.67	3.39	0.70	6.90	8.2	7.8
7 Colombia 1979	16	1.67	3.72	1.09	6.91	8.2	7.7
8 Mindanao 1976	16	2.08	2.68	0.99	7.26	8.1	7.8
9 Peru 1974	17	1.94	3.06	0.58	7.00	8.1	7.6
10 Santa Cruz Island 1980	20	1.64	2.35	0.86	6.79	7.8	7.7
11 Oaxaca 1978	17	2.18	2.35	0.35	6.87	7.6	7.8
12 Petatlan 1979	18	1.81	2.37	0.32	6.71	7.6	7.6
13 Tangshan 1976	21	1.55	3.47	0.29	6.76	7.45	7.7
14 Guatemala 1976	17	1.56	3.88	0.89	6.66	7.5	7.5
15 Turkey 1976	17	1.78	2.06	0.22	6.58	7.2	7.3
16 Turkey 1967	22	1.51	2.06	0.21	6.38	7.4	7.1
17 San Fernando 1971	26	1.26	0.82	0.03	6.41	6.6	6.7
18 Imperial Valley 1979	19	1.60	1.75	0.30	5.92	6.5	6.5

* For the Rat Island 1965 earthquake, T_M has a bimodal distribution: $T_M = 0.77 \pm 0.30$ and $T_M = 2.31 \pm 0.26$.

that we measured can be seen in Figure 4c. We also measured T_M, the time between the first arrival of energy and the time of the maximum amplitude, and C, the coda length, which we define as the time from the first arrival until the peak-to-peak amplitude on the record has decreased to $A/2$; that is, until the amplitude has decreased to about 25 per cent of its maximum value. Examples of picks of T_M and C are shown in Figure 1. Table 1 presents average values of T, C, T_M, and $\hat{m}_b$ for each event. Moment magnitude, M_w, and surface-wave magnitude, M_S, are also listed for comparison (mostly taken from Lay *et al.*, 1982). All events in Table 1 are subduction-zone thrust events except: no. 4, which is an intraplate normal faulting event at the trench; nos. 13 to 18, which are strike-slip events; and no. 17, which is an intraplate thrust event. A comparison of m_b and M_S for about 50 earthquakes with M_S of 5.0 to 7.5 indicates that for a given M_S, thrust earthquakes have m_b about $\frac{1}{4}$ units higher on the average than strike-slip earthquakes (Eissler and Kanamori, 1985).

The quality of the WWSSN records is very uneven. The standard deviations in $\hat{m}_b$ values are about 0.25, which is typical of most magnitude scales. The period, T, is the most difficult parameter to measure and, since the gain of the instrument depends on the period, uncertainty in T may account for some of the scatter in $\hat{m}_b$.

Figure 2 shows that unlike m_b, $\hat{m}_b$ does not appear to saturate completely with increasing M_w. For example, m_b for the 1964 Alaskan earthquake is 6.4, while $\hat{m}_b$ is 7.6. A least-squares fit to the data shown in Figure 2 yields the following relationship between $\hat{m}_b$ and M_w

$$\hat{m}_b = 0.53M_w + 2.70 \tag{2}$$

for M_w from 6.5 to 9.5. Since M_w is defined by $M_w = (\log M_0 - 16.1)/1.5$, (1) and (2) imply, assuming T is constant, that

$$A_g \propto M_0^{0.35} \tag{3}$$

where M_0 is the seismic moment.

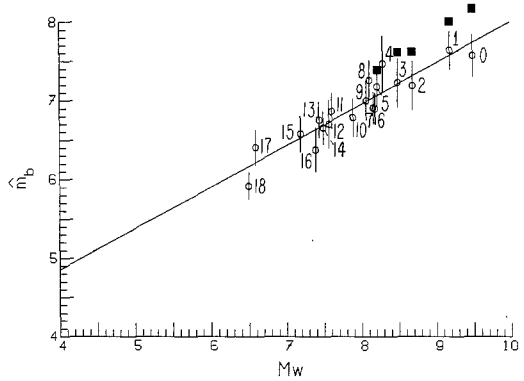

FIG. 2. $\hat{m}_b$ versus M_w. The vertical bars show the standard deviations around the average $\hat{m}_b$ value. The number next to each data point refers to the event number in Table 1. The straight line was obtained by a least-squares fit to the data and follows: $\hat{m}_b = 0.53\ M_w + 2.70$. The black squares represent the results of the simulation procedure discussed later in the text. The events simulated are nos. 0, 1, 2, 3, and 5 in Table 1. The subevent is no. 17.

Figure 3a shows a general increase in coda length with increasing M_w. Intuitively, the coda length should be proportional to fault length. In Figure 3b, C is plotted against the rupture time (i.e., fault length, L, divided by rupture velocity, V). The coda length has a large scatter because of contamination by aftershocks, different receiver effects, and, occasionally, the arrival of the phase PP. Nevertheless, the data support the interpretation that the coda is roughly equal to the rupture time plus a constant time. The reference line in Figure 3b represents the relationship $C = L/V + 1.5$ min. We take $V = 2.5$ km/sec, which is typical of the rupture velocities summarized in Lay *et al.* (1982). Fault plane dimensions are generally taken from Lay *et al.* (1982). The extra 1 to 1.5 min is probably partly caused by scattering at the source and at the receiver. It may also result from the contaminating effects mentioned above, or from our particular definition of coda length.

In a general sense, the increase of T_M with M_w seen in Figure 4a can be explained if we view the occurrence of the maximum amplitude as a statistical event that is composed of arrivals from various parts of a uniformly rough fault plane. In this case, T_M should increase linearly with the length and width of the rupture zone,

hence its increase with M_w. However, the deviation of T_M from a steady increase with M_w can be interpreted by considering the large-scale asperities (here defined as stronger regions with higher than average moment release per unit area). If asperities are important in releasing short-period energy, the distribution of moment

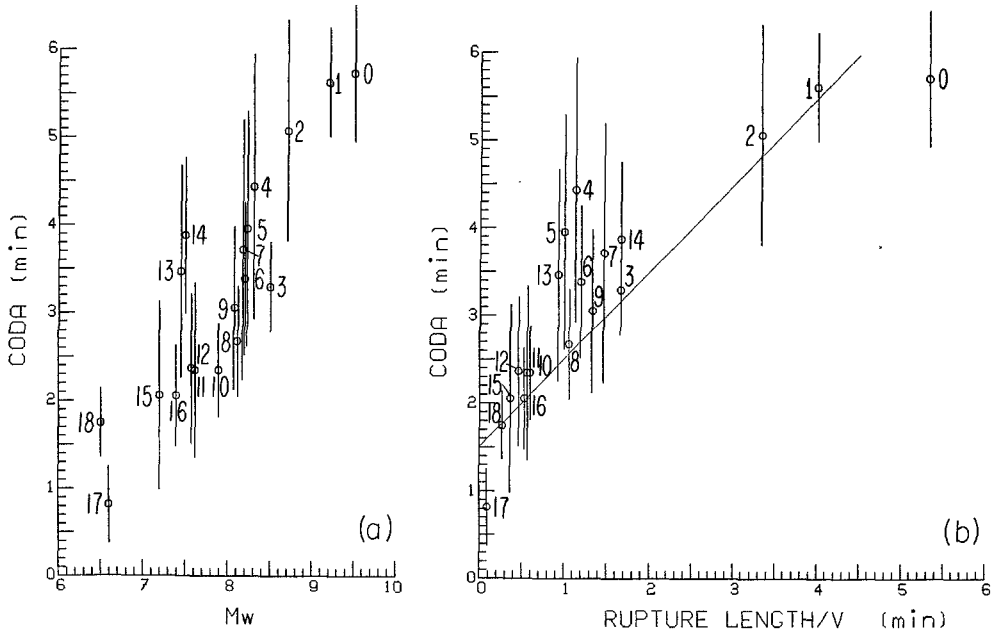

FIG. 3. (a) Coda length versus M_w. The vertical bars show the standard deviations around the average coda value. The number next to each data point refers to the event number in Table 1. (b) Coda length versus rupture time. The reference line shows the relation: coda length = rupture length/V + 1.5 min where V = rupture velocity = 2.5 km/sec (see text).

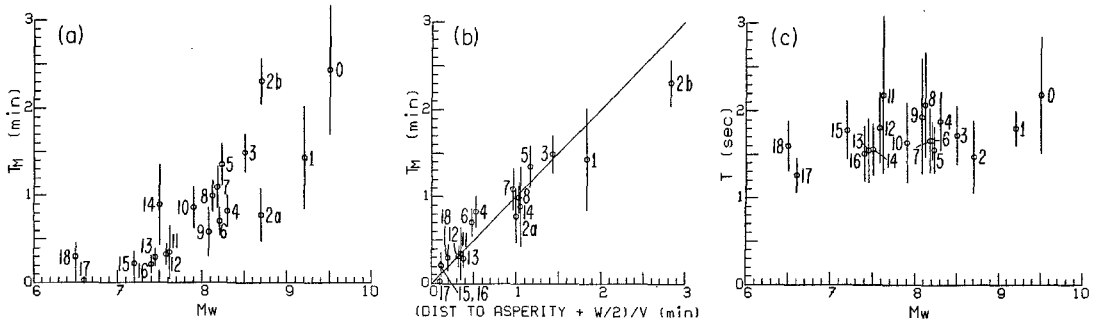

FIG. 4. (a) Time from the beginning of the P wave until the maximum amplitude is achieved, T_M versus M_w. The vertical bars show the standard deviations in T_M. The number next to each data point refers to the event number in Table 1. (b) T_M versus time for rupture to propagate from hypocenter to largest asperity (see text). The reference line of slope 1 represents (4). (c) Period at maximum amplitude versus M_w. The vertical lines show the standard deviations in the period.

release will interact statistically with random receiver or path effects to control T_M. On average, T_M should be proportional to the distance between the hypocenter and the most significant asperity. Figure 4b shows measured T_M with standard deviation bars plotted against our estimate of the time between the initiation of rupture and the production of the maximum moment release per unit time. This quantity is estimated by adding the distance, D, from the hypocenter to the middle of the

largest asperity to half of the width of the fault plane, W, and dividing the sum by the rupture velocity, V

$$\text{estimated } T_M \approx \frac{D + W/2}{V}. \tag{4}$$

Here, we envision that after the rupture front arrives at a point, the slip motion there continues for W/V sec. Then $W/2V$ is half the duration of the slip motion. If the hypocenter is located within the largest asperity, then D is taken to be the radius of the asperity.

The positions of the asperities are inferred from studies in which long-period WWSSN records are deconvolved to yield the location in time and space of the areas on the fault plane that generate the most long-period radiation (with periods of 10 to 50 sec). The moment release has been mapped by such methods for most of the earthquakes we are examining (Kanamori and Stewart, 1978; Langston, 1978; Butler *et al.*, 1979; Stewart and Cohn, 1979; Chael and Stewart, 1982; Kikuchi and Kanamori, 1982; Ruff and Kanamori, 1982; Stewart and Kanamori, 1982; Hartzell and Heaton, 1983; Beck and Ruff, 1984, 1985; Kikuchi, written communication, 1984).

For each earthquake, T_M is an average. Earthquake no. 2 (Rat Island, 1965) possesses a markedly bimodal distribution of T_M that is quite consistent with Kikuchi's and with Ruff and Kanamori's (1983) pattern of asperities. Both deconvolutions show two large asperities, one near the hypocenter and the other at the far end of the fault plane. Therefore, we separated the T_M's for Rat Island, 1965, into two groups ($T_M = 0.77 \pm 0.31$ min and $T_M = 2.31 \pm 0.26$ min and calculated two estimated T_M's based on the distances to the two asperities. The results are plotted in Figure 4b as points 2a and 2b. The generally good agreement in Figure 4b between the data and our estimate suggests that short-period radiation is, on average, generated preferentially in the same regions of the fault plane as longer period radiation (with periods of 10 to 50 sec).

The period at the maximum amplitude, T, is plotted against moment magnitude, M_w, in Figure 4c. T is longer than 0.7 sec, the period of the peak in the WWSSN short-period response curve, because the instrument response is multiplied in the frequency domain by a source spectrum that increases as period increases. Figure 4c suggests that despite large scatter, T remains almost constant as M_w increases. The two smallest earthquakes (San Fernando, 1971 and Imperial Valley, 1979) have shorter periods. It should be noted that T is usually about 0.4 sec longer than the average period of the P wave (Boore, 1986).

GDSN Data

Several theoretical studies have been made to relate the seismic source spectrum to rupture processes (Haskell, 1964, 1966; Aki, 1967; Brune, 1970). Also, many investigators have estimated the source spectrum empirically (e.g. Aki, 1972, 1983; Gusev 1983). Various spectral models have been proposed, both theoretically and empirically. Important differences exist between these models. Previous empirical approaches to obtaining source spectra have been indirect, often deduced from comparisons of m_b, M_S, and other magnitude scales. Since m_b is a measurement at one period, and since it is determined from the first few cycles of the P-wave train only, it does not always represent the source spectrum correctly.

Since the nature of the source spectrum is important to understand the earthquake rupture process and for empirical prediction of strong ground motion (as in Boore,

1983), we investigate this problem by using records from GDSN. We study seven earthquakes recorded by GDSN including five large subduction-zone thrust events (1983 Akita-Oki, 1980 Santa Cruz Islands, 1983 North Chile, 1982 Tonga Island, and 1983 Costa Rica), a normal-faulting event (1983 Chagos Ridge), and a California thrust event (1983 Coalinga). We also analyze teleseismic hand-digitized WWSSN records of the 1971 San Fernando earthquake used by Langston (1978). The events and the stations used for each event are listed in Table 2.

We analyze intermediate-period records from DWWSSN and RSTN stations, and short-period records from DWWSSN, SRO, and ASRO stations. The short-period DWWSSN, SRO, and ASRO instrument responses peak between 0.5 and 0.7 sec and fall off about as ω^{-2} between 1 and 0.1 Hz (1 and 10 sec). The broadband intermediate-period DWWSSN and RSTN responses peak at 1 sec, but fall off only as ω^{-1} between 1 and 0.1 Hz. Ninety records are used. We use only unclipped or slightly clipped records.

For the well-recorded Akita-Oki event, excellent coherence is observed from station to station, and between the intermediate- and short-period records at a given station. Figure 5 shows some of these records. We window, taper, and Fourier transform the P-wave train. The window length is given by the coda length as defined in our analysis of WWSSN records above. Typical coda lengths are 1 to 3 min.

After removing the appropriate instrument response from the spectra, we correct for attenuation with a constant $t^* = 0.7$ sec where t^* is the P-wave attenuation parameter defined by $t^* = \int ds/Q(s)\alpha(s)$. Here, $Q(s)$ and $\alpha(s)$ are the quality factor and the P-wave velocity along the ray path s, and the integral is taken along s.

Admittedly, t^* depends on station distance (Kanamori, 1967), frequency (Der and Lees, 1985), and tectonic province (Der and Lees, 1985). However, in the interest of simplicity and because the detailed behavior of t^* is not well known for all the source-station paths used in this study, we chose a constant t^*. The effect of using Der and Lees' (1985) QPST model for t^* compared to using a constant $t^* = 0.7$ sec is to lower the spectral amplitude at the source by a factor of 1.1 at 2 sec and by a factor of 1.6 at 1 sec. Spectral amplitudes are not significantly affected at periods longer than 2 sec.

Another frequency-dependent effect is the amplification of waves as they travel toward the surface through material of decreasing velocity. This effect is discussed by Boore (1986) and Gusev (1983). It tends to amplify short-period waves more than long-period waves, and, therefore, operates in the same direction as Der and Lees' (1985) frequency-dependent t^*. Boore (1986) estimates that the near-surface amplification effect will increase 1-sec amplitudes by a factor of 1.32 more than 10-sec amplitudes. Gusev (1983) finds this factor to be 1.78. Ten-second energy is amplified by a factor of only 1.10 according to Boore (1986) and not at all according to Gusev (1983). Since it depends on the station site, we chose to ignore it. Because of the neglect of the frequency dependence of t^* and the near-surface amplification effect, spectral amplitudes at 1 sec could be slightly uncertain. However, our estimate of the spectral amplitudes at periods longer than 2 sec is considered reliable.

Each spectrum is further corrected for distance (geometrical spreading), radiation pattern, and free-surface receiver effect. Then, for each earthquake, 6 to 16 corrected spectra are averaged together in a logarithmic sense (i.e., we average the logarithm of the spectral amplitude). We thus obtain the average moment rate spectrum, or

equivalently, moment rate spectral density, $\hat{\dot{M}}(\omega)$, for each earthquake according to

$$\hat{\dot{M}}(\omega) = \frac{4\pi\rho\alpha^3 R_E}{g(\Delta)R_{\theta\phi}C}\left[\frac{e^{\frac{\omega t^*}{2}}}{\hat{I}(\omega)}\hat{u}(\omega)\right] \tag{5}$$

where ρ and α are the density and P-wave velocity at the source, R_E is the radius of the earth, $g(\Delta)$ represents geometrical spreading, $R_{\theta\phi}$ is the effective radiation pattern of the P-wave train that includes the P, pP, and sP phases, C is the free-surface receiver effect, t^* represents attenuation, $\hat{I}(\omega)$ is the instrument response, and $\hat{u}(\omega)$ is the observed displacement spectrum. The symbol "^" in (5) denotes a Fourier-transformed quantity.

In all these events, the crust is involved in faulting. Hence, we take $\rho = 2.8$ gm/cm^3 and $\alpha = 6.5$ km/sec for the larger events, and $\rho = 2.65$ gm/cm^3 and $\alpha = 6.1$ km/sec for the California events. Geometric spreading, $g(\Delta)$, is taken from Kanamori and Stewart's (1976) Figure 8. The radiation pattern and free-surface receiver effect, $R_{\theta\phi}$ and C, are computed from the station distance and azimuth and the focal mechanism of the event. The effective radiation pattern, $R_{\theta\phi}$, is obtained by first computing the amplitudes of the P, pP, and sP phases at the station using equation (8) of Kanamori and Stewart (1976), and then taking the root-mean-square value. A similar procedure is used by Boore and Boatwright (1984).

In reality, the three phases will interfere to yield a frequency-dependent radiation pattern. However, this is not important in an average sense, especially for extended ruptures. To show this, we divide a dipping fault plane into subfaults, choose the point where rupture begins, and let rupture propagate with an average rupture velocity. For each subfault, we calculate the amplitudes of the P, pP, and sP phases (which depend on the fault mechanism) and the time delays of the pP and sP phases after P (which depend on the depth of the subfault and the position of the receiver). We sum the arrivals in time (each arrival is simply a spike), Fourier transform, and divide the spectrum by the spectrum of the P arrivals only, to normalize it. The resulting spectrum is essentially the radiation pattern as a function of frequency. Figure 6 shows the average of eight such spectra computed at different azimuths for a thrust mechanism on a 150 km × 70 km fault plane dipping 30° divided into 105 subfaults. The average radiation pattern ratio exhibits little frequency dependence and matches the average scalar radiation pattern ratio, $\sqrt{(R^P)^2 + (R^{pP})^2 + (R^{sP})^2}/R^P$, where R^X represents the amplitude of the phase X. This justifies our use of a frequency-independent radiation pattern.

The spectrum of each record in Table 2 is corrected according to (5). Then, for each earthquake, the corrected spectra are averaged and shown in Figures 7 and 8. Theoretical spectra for an ω^{-2} model are shown as a reference [for a description of the model, see equation (8)]. The spectral values at the low-frequency end of the spectrum in Figures 7 and 8 were obtained from the scalar seismic moments determined from long-period waves. The standard deviations of the averages are shown by vertical bars. The scatter seems to be caused by path and receiver-site effects, since removing the effects of distance, distance-dependent t^*, radiation pattern, and the free-surface receiver effect caused the standard deviations to decrease less than 20 per cent. In this connection, Koyama and Zheng (1985) have

TABLE 2

RECORDS USED IN SPECTRAL ANALYSIS

Station	Type	Δ (°)	Azimuth (°)	$R_{\theta\phi}$	C
Akita-Oki, Japan 26 May 1983 $M_w = 7.8$					subduction thrust
CTAO	SP ASRO	60.7	172.3	0.80	1.79
KONO	SP ASRO	71.9	335.7	0.86	1.84
COL	IP DWWSSN	47.2	33.7	1.41	1.73
LON	IP DWWSSN	67.2	47.3	1.44	1.81
HON	IP DWWSSN	56.0	89.8	1.64	1.76
KEV	IP DWWSSN	59.6	338.1	0.81	1.79
AFI	IP DWWSSN	70.7	128.8	1.17	1.83
BER	IP DWWSSN	72.6	338.0	0.87	1.84
TAU	IP DWWSSN	83.4	173.9	0.93	1.88
RSNT	IP RSTN	62.7	30.3	1.31	1.80
RSSD	IP RSTN	78.4	40.9	1.30	1.87
RSNY	IP RSTN	90.0	23.3	1.16	1.90
RSON	IP RSTN	77.9	31.0	1.24	1.87
Santa Cruz Islands 17 July 1980 $M_w = 7.8$					subduction thrust
CHTO	SP SRO	73.0	294.2	0.98	1.84
NWAO	SP SRO	48.8	237.1	0.78	1.73
TATO	SP SRO	57.2	310.8	0.91	1.77
MAJO	SP ASRO	55.4	332.9	0.98	1.76
SNZO	SP SRO	29.8	166.5	0.93	1.63
GUMO	SP SRO	33.3	320.4	0.82	1.65
Chagos Ridge, Indian Ocean 30 November 1983 $M_w = 7.7$					Normal
GUMO	SP SRO	75.0	74.0	0.84	1.85
NWAO	SP SRO	49.2	128.1	0.76	1.73
KONO	SP ASRO	82.6	332.9	1.32	1.88
KEV	IP DWWSSN	82.5	345.6	1.29	1.88
SLR	IP DWWSSN	45.8	240.6	0.86	1.71
TAU	IP DWWSSN	74.5	132.5	0.93	1.85
North Chile 4 October 1983 $M_w = 7.6$					subduction thrust
SCP	IP DWWSSN	67.6	354.2	0.77	1.82
LON	IP DWWSSN	86.5	327.5	0.72	1.89
SLR	IP DWWSSN	86.2	116.9	1.19	1.89
TOL	IP DWWSSN	90.8	45.1	1.23	1.91
ANMO	SP SRO	70.0	329.3	0.62	1.83
SNZO	SP SRO	89.1	223.2	0.96	1.90
JAS	SP DWWSSN	79.4	322.1	0.70	1.87
Tonga-Kermadec Trench 19 December 1982 $M_w = 7.5$					subduction thrust
COL	SP DWWSSN	91.5	11.6	0.84	1.91
LON	SP DWWSSN	85.9	34.0	0.85	1.89
JAS	SP DWWSSN	80.8	41.3	0.86	1.87
TAU	SP DWWSSN	35.6	229.2	1.49	1.66
ANMO	SP SRO	88.2	50.4	0.92	1.90
CTAO	SP ASRO	35.3	269.0	1.97	1.66
Costa Rica 3 April 1983 $M_w = 7.4$					subduction thrust
SCP	IP DWWSSN	32.3	7.5	1.92	1.64
COL	IP DWWSSN	71.5	336.0	1.35	1.84

TABLE 2—*Continued*

LON	IP DWWSSN	50.2	326.0	1.35	1.74
TOL	IP DWWSSN	76.0	51.1	1.33	1.86
BER	IP DWWSSN	81.7	30.1	1.42	1.88
ANMO	SP SRO	33.6	324.1	1.39	1.65
GRFO	SP SRO	86.2	40.4	1.32	1.89
ZOBO	SP ASRO	29.0	149.1	0.54	1.62
KONO	SP ASRO	83.9	30.7	1.39	1.89
HON	SP DWWSSN	72.8	289.6	0.87	1.84
KEV	SP DWWSSN	88.6	19.1	1.37	1.90
AFI	SP DWWSSN	90.1	256.2	0.86	1.91
RSCP	IP RSTN	26.9	355.6	1.86	1.61
RSSD	IP RSTN	39.7	336.3	1.56	1.68
RSNY	IP RSTN	36.5	10.4	1.91	1.66
RSON	IP RSTN	43.0	350.2	1.72	1.70
Coalinga 2 May 1983 $M_w = 6.4$					intraplate thrust
ZOBO	SP ASRO	71.9	126.9	0.91	1.84
MAJO	SP ASRO	77.2	306.1	1.40	1.86
KONO	SP ASRO	75.7	23.6	0.98	1.85
SCP	SP DWWSSN	33.2	70.0	0.54	1.64
HON	SP DWWSSN	40.0	256.1	1.14	1.68
KEV	SP DWWSSN	71.5	11.4	1.14	1.84
AFI	SP DWWSSN	69.7	234.3	0.88	1.83
COL	IP DWWSSN	33.0	338.8	1.79	1.64
San Fernando 9 February 1971 $M_w = 6.6$					intraplate thrust
BLA	SP WWSSN	30.8	73.7	0.92	1.63
AFI	SP WWSSN	69.9	236.1	1.10	1.83
MAT	SP WWSSN	79.7	307.2	1.07	1.87
KEV	SP WWSSN	73.1	11.9	0.89	1.84
NUR	SP WWSSN	80.7	17.6	0.96	1.87
KTG	SP WWSSN	60.1	22.7	0.79	1.79
PTO	SP WWSSN	80.9	46.0	0.99	1.88
OGD	SP WWSSN	34.9	65.9	0.89	1.65
GIE	SP WWSSN	42.5	135.9	1.27	1.70
PEL	SP WWSSN	80.7	141.6	1.26	1.87
KIP	SP WWSSN	37.1	260.2	0.90	1.67
NAT	SP WWSSN	87.2	98.5	1.18	1.90
BHP	SP WWSSN	43.6	116.2	1.17	1.70
ARE	SP WWSSN	67.4	130.7	1.23	1.82
HNR	SP WWSSN	88.5	257.6	1.12	1.90
ALE	SP WWSSN	51.8	8.0	0.72	1.75
AQU	SP WWSSN	91.8	33.6	1.06	1.91
ATL	SP WWSSN	28.2	82.3	0.96	1.62
CUM	SP WWSSN	54.4	102.2	1.11	1.76
ESK	SP WWSSN	74.9	32.4	0.92	1.85
GDH	SP WWSSN	49.4	25.1	0.75	1.73
KON	SP WWSSN	76.9	24.3	0.93	1.86
STU	SP WWSSN	85.0	31.7	1.00	1.89
TRI	SP WWSSN	89.3	31.4	1.04	1.90
FBC	SP WWSSN	42.2	30.4	.76	1.69
SCH	SP WWSSN	40.9	43.8	0.80	1.69
STJ	SP WWSSN	49.8	53.8	0.85	1.74
FCC	SP WWSSN	29.2	26.0	0.77	1.62

observed that short-period P waves do not follow the P-wave radiation pattern. Considering the uncertainties in our method of reduction and the scatter in the data, we must be careful not to overinterpret the results. However, it is evident in Figure 7 that the Tongan earthquake has proportionally less high-frequency energy than do the other five events. This can be interpreted as the result of weaker coupling of the subduction interface caused by the greater age and density of the subducting sea floor (Ruff and Kanamori, 1980). The Costa Rica earthquake falls between the Tongan and Akita-Oki events.

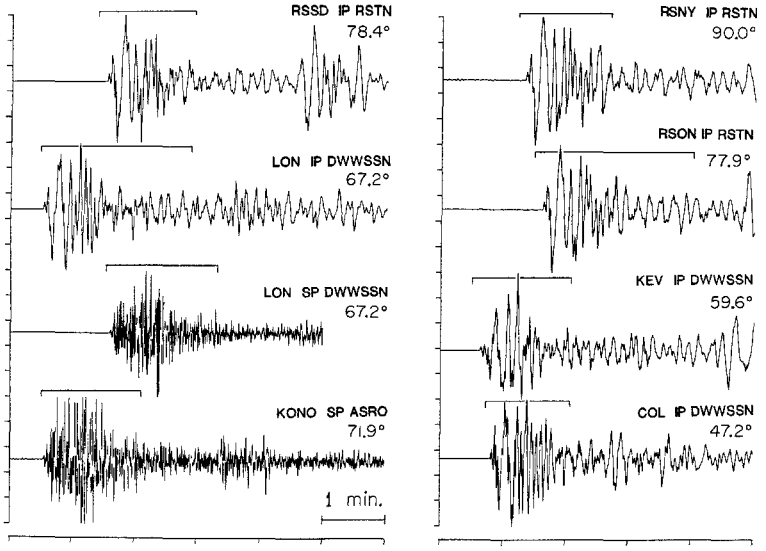

FIG. 5. Examples of digital intermediate- and short-period seismograms from the GDSN Network for the 1983 Akita-Oki earthquake. For each record, instrument type and distance are given. Brackets show the portion of the P wave that is windowed and Fourier-transformed.

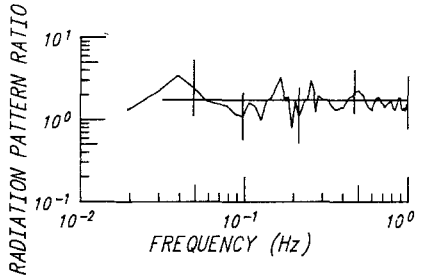

FIG. 6. Average radiation pattern ratio as a function of frequency for an extended fault model in a half-space. We divide $[P + pP + sP](\omega)$ by $P(\omega)$ for each of eight azimuths and average the results around an extended thrust event on a fault-plane that dips 30°. The vertical lines show standard deviations of the average at selected frequencies. The horizontal line represents the average of the ratios of the scalar radiation pattern ratio, $\sqrt{(R^P)^2 + (R^{pP})^2 + (R^{sP})^2}/R^P$. The good comparison justifies our use of the frequency-independent scalar radiation pattern in computing the source spectrum.

Figure 8 shows source spectra of the two California events (Coalinga and San Fernando) with the ω^{-2} spectral model as a reference. Figures 7 and 8 illustrate the pitfalls of considering only spectral slopes or approximating the ω^{-2} model by a line of slope 0 and a line of slope -2. The roll-off actually occurs over nearly a decade in frequency. A straight line fit to the Akita-Oki spectrum by least squares between 0.1 and 1 Hz has a slope of -1.75, but it is evident from Figure 7 that the Akita-Oki spectrum is close to the ω^{-2} model.

Relation Between $\hat{m}_b$ and Spectral Amplitude

We can obtain source spectra from GDSN records as described above only for recent earthquakes; the largest earthquake that was well-recorded on GDSN has $M_w = 7.8$. For great earthquakes, only $\hat{m}_b$'s measured from WWSSN records are available. In this section, we use the $\hat{m}_b$ data to estimate spectral amplitudes at

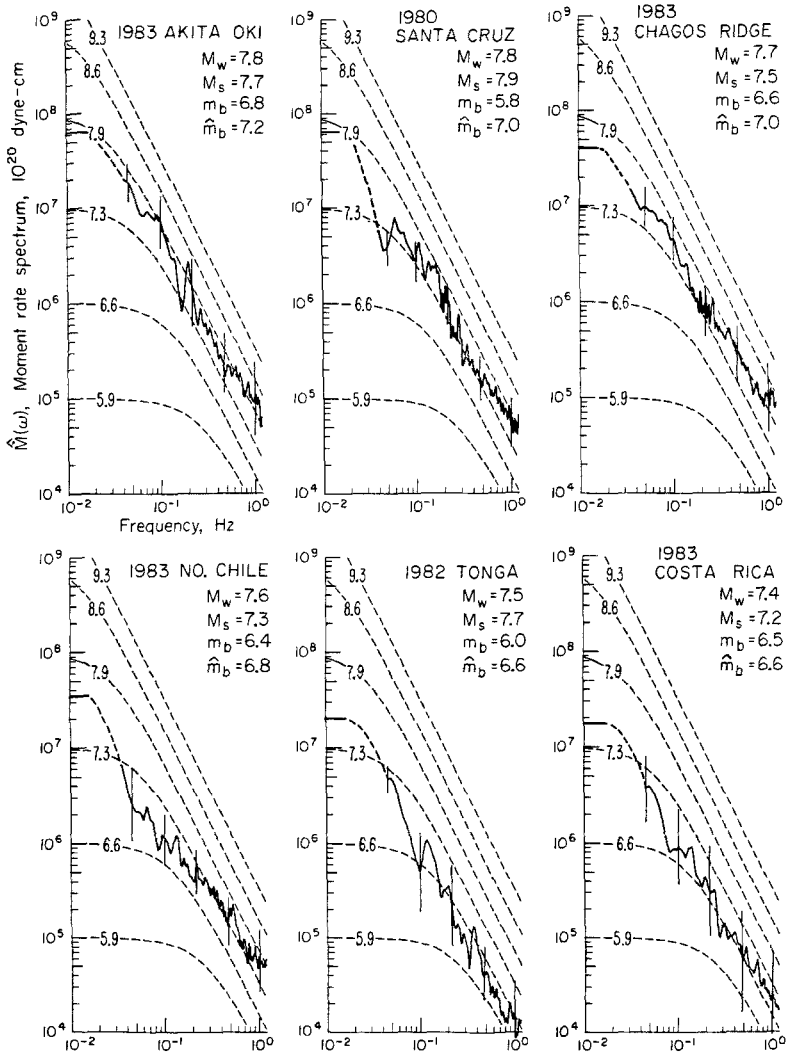

FIG. 7. Comparison of the average moment rate spectra for six earthquakes. The dashed curves show theoretical spectra for an ω^{-2} model. These curves are shown as a reference. The spectral values at the low-frequency end were obtained from the scalar seismic moment determined from long-period waves. The vertical bars show standard deviations at selected frequencies.

short periods. For $M_w = 9.0$ and 8.0, we estimate an average $\hat{m}_b = 7.48$ and 6.95, respectively, from (1), and an average period, $T = 1.8$ sec, from Figure 4c. We fix the distance, Δ, at about the average of the station distances used to calculate $\hat{m}_b$; we take $\Delta = 75°$. Then, (1) gives the average maximum ground displacement from body waves, $A_g = 10.8\mu$ and 5.1μ, at $\Delta = 75°$ for $M_w = 9.0$ and 8.0, respectively.

The conventional procedure for relating time-domain amplitude of a signal to its

spectral amplitude is to postulate that

$$\hat{u}(\omega_0) \propto AC_D^m \tag{6}$$

where A is the maximum amplitude in the time domain, $\hat{u}(\omega_0)$is spectral amplitude at the angular frequency where A is measured or defined, and C_D is some measure of the duration of the signal. For well-dispersed waves (e.g., 20-sec surface waves), m can be taken to be 0 (Aki, 1967). However, the appropriate value for m in (6) is not obvious for complex short-period body waves. If the wave train is approximated by a sine wave modulated by a Gaussian envelope of amplitude A and duration C_D, then (6) applies with $m = 1$. That approximation naturally produces a very sharp spike in the spectrum, and ignores the random nature of short-period waves. If the wave train is approximated by a random signal of maximum amplitude A and duration C_D with an appropriate bandwidth, then in (6), m is 0.5 [Koyama and Zheng, 1985, equation (A12)].

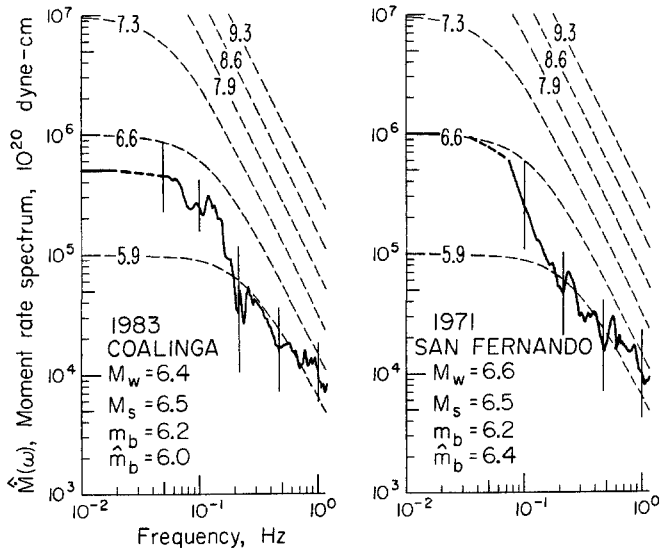

FIG. 8. Moment rate spectra for two California earthquakes. See legend to Figure 7.

We prefer an empirical approach to estimate $\hat{u}(\omega_0 = 2\pi/T)$ from A. For the digital data, both time-domain and spectral amplitudes are known, so we plot $\log[A/\hat{u}(\omega_0)]$ versus M_w in Figure 9. We use available short-period records from the GDSN stations listed in Table 2, as well as short-period GDSN records of the 1984 Morgan Hill, California, 1978 Oaxaca, 1979 Petatlan, and 1979 Colombia earthquakes. The last three events are included in Table 1. Two hand-digitized records are used: the 1964 Alaskan earthquake recorded by a Wood-Anderson seismograph at Pasadena, California, and the 1960 Chilean earthquake recorded by a Willmore short-period vertical seismograph at Halifax, Canada. The Wood-Anderson response is deconvolved from the 1964 Alaska record, and a standard short-period DWWSSN response is convolved with the resulting ground displacement. The simulated short-period record is then treated like the GDSN records. We obtain two values of log

$[A/\hat{u}(\omega_0)]$ from Figure 9 that correspond to $M_w = 8.0$ and $M_w = 9.0$ and are shown by X's.

The reference line in Figure 9 represents (6) with $m = 0.25$. This can be seen by applying the standard scaling relation between moment and length, ($M_0 \propto L^3$), and the proportionality between fault length and coda duration demonstrated in Figure 3b. Although the data for great earthquakes are sparse, m does not seem to be a strong function of M_w or C, so that (6) may be a valid assumption. From Figure 9, m appears to be significantly less than 0.5.

Finally, the moment rate spectral density, $\hat{M}(\omega_0)$, is calculated from $\hat{u}(\omega_0)$ by (5) using the following parameters: as before, $\rho = 2.8$ gm/cm^3 and $\alpha = 6.5$ km/sec, $g(\Delta) = 0.3$, $C = 1.8$, $R_{\theta\phi} = 1.0$, and $t^* = 0.7$ sec. The moment rate spectral densities thus estimated from $\hat{m}_b$ and T are

$$\hat{M}\left(0.55 \text{ Hz} = \frac{1}{1.8 \text{ sec}}\right) = \begin{cases} 8.8 \times 10^{25} \text{ dyne-cm} & \text{for } M_w = 9.0 \\ 1.9 \times 10^{25} \text{ dyne-cm} & \text{for } M_w = 8.0. \end{cases} \quad (7)$$

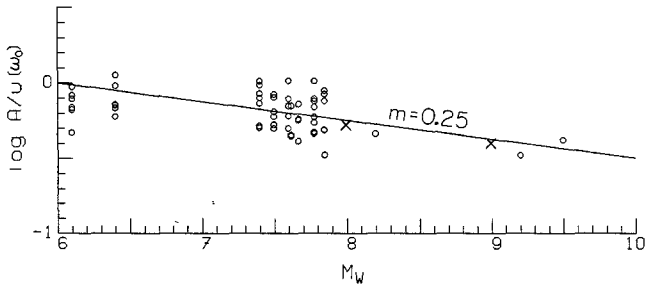

FIG. 9. The open circles show the ratio of maximum time-domain amplitude to spectral amplitude for each short-period record as a function of M_w. A is time-domain amplitude at period, T, and $u(\omega_0)$ is frequency-domain amplitude at $\omega_0 = 2\pi/T$. The X's show the ratios used in this study to estimate spectral amplitudes from $\hat{m}_b$. The reference line shows $m = 0.25$ [see (6) in text].

In the same way that (7) was determined, we can determine $\hat{M}$ (0.55 Hz) for the 1964 Alaskan earthquake ($M_w = 9.2$). From Table 1, $\hat{m}_b$ is 7.64, and T is 1.81 sec. Therefore, A_g is 12.5 μm at a distance of 75°. We choose $\log[A/u(\omega_0)] = -0.44$ from Figure 9. Then for the 1964 Alaskan earthquake

$$\hat{M}(0.55 \text{ Hz}) = 1.3 \times 10^{26} \text{ dyne-cm}$$

in contrast to Koyama and Zheng's (1985) estimate of 1.7×10^{27} dyne-cm (at 1.4 sec, Koyama, written communication). Koyama and Zheng's estimate is larger than ours for two main reasons. First, they use a t^* of about 1.4 sec compared to our t^* of 0.7 sec. This difference tends to overestimate the source spectrum. In addition, their estimate of spectral density from time-domain amplitude is based on their equation (A12), which overestimates the spectrum by a factor of 1.5 to 2 (see Koyama and Zheng, 1985, Figure A3). Our estimate of $\hat{M}$ (0.55 Hz) from $\hat{m}_b$ from the 1964 Alaskan earthquake is consistent with (1.3 times larger than) the spectrum obtained from the Pasadena Wood-Anderson record of the 1964 Alaskan earthquake (see the next section and Figure 11c).

Discussion: Comparison of Data with Spectral Models

Figure 10 compares four spectra from GDSN records and the spectral amplitudes that we estimated from the $\hat{m}_b$ data to an ω^{-2} spectral model given by

$$\hat{M}(\omega) = \frac{M_0 {\omega_c}^2}{{\omega_c}^2 + \omega^2} \quad \text{with corner frequency,} \quad \frac{\omega_c}{2\pi} = 0.49\beta\left[\frac{\Delta\sigma}{M_0}\right]^{\frac{1}{3}} \tag{8}$$

with stress parameter, $\Delta\sigma = 30$ bars and S-wave velocity, $\beta = 3.75$ km/sec (Brune, 1970). The spectral amplitudes estimated from $\hat{m}_b$ and given in (7) are shown in

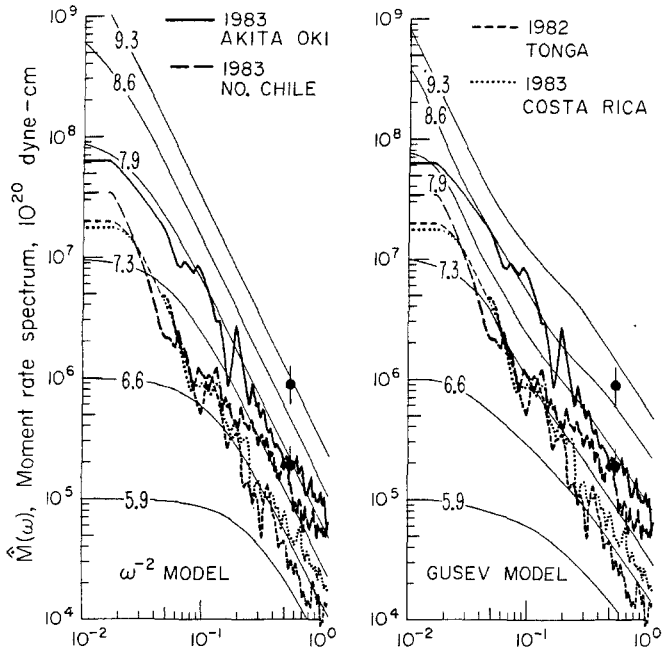

FIG. 10. Comparison of the spectra of four earthquakes and spectral amplitudes estimated from the $\hat{m}_b$ data with ω^{-2} and Gusev spectral models. The two dots show the spectral amplitudes at 0.55 Hz estimated from $\hat{m}_b$ for $M_w = 8.0$ and $M_w = 9.0$. The vertical bars show the uncertainty associated with the standard error of the estimate in $\hat{m}_b$ versus M_w, $\pm$ 0.17.

Figure 10 by dots whose error bars represent the change in $\hat{M}(\omega_0)$ associated with a change of $\pm$ 0.17 in $\hat{m}_b$, which is the standard error of the estimate of the least squares fit to $\hat{m}_b$ versus M_w. Figure 10 also compares the same data to the Gusev source spectral model. The Gusev spectral model was constructed empirically from a synthesis of different magnitude relations (Aki, 1972, 1983; Gusev, 1983). Hence, it is a more complicated model than the ω^{-2} model, as shown by its lack of similitude. For large moments, the Gusev model predicts decreased amplitudes at 10 to 20 sec and enhanced amplitudes at about 2 sec compared to the ω^{-2} model with $\Delta\sigma = 30$ bars. Of the digitally recorded events, the Alita-Oki earthquake fits the ω^{-2} model better than it fits the Gusev model, the Costa Rica earthquake fits the Gusev model better, and the Tonga earthquake has a faster spectral fall-off than the ω^{-2} model.

From the definition of M_w, the spacing of the spectral amplitudes in (7) for M_w

= 8.0 and 9.0 yields

$$\hat{M}\left(0.55 \text{ Hz} = \frac{1}{1.8 \text{ sec}}\right) \propto M_0^{0.45}. \tag{9}$$

An exponent of $\frac{1}{3}$ would be consistent with the spectral fall-off of -2 associated with an ω^{-2} model. The exponent of 0.45 in (9) suggests a spectral fall-off of -1.7. However, to fit the absolute levels in (7) to an $\omega^{-1.7}$ model defined in a fashion similar to (8), the $\Delta\sigma$ in (8) would need to be much smaller than 30 bars. A comparison of (9) with (3) and (6) suggests that m in (6) is about 0.3, providing a further indication that m in Figure 9 is significantly smaller than 0.5.

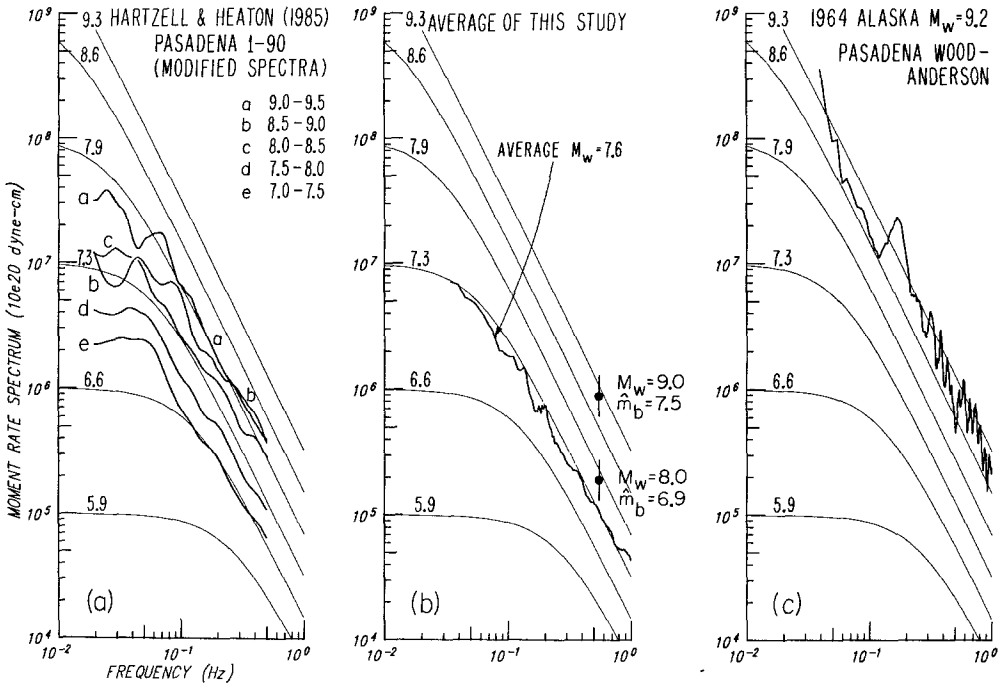

FIG. 11. (a) Averages of the source spectra of 61 Pasadena, California, Benioff 1-90 records. The earthquakes have been grouped into five magnitude ranges: M_w = 7.0 to 7.5, 7.5 to 8.0, 8.0 to 8.5, 8.5 to 9.0, and 9.0 to 9.5. The smoothed spectra in each group have been averaged together. The ω^{-2} spectral model described in (8) is shown for reference. This figure can be compared with Hartzell and Heaton's (1985) Figure 11a. (b) The average of the source spectra of the six earthquakes in Figure 7. The average M_w is 7.63. The two dots show the spectral amplitudes at 0.55 Hz estimated from $\hat{m}_b$ for M_w = 8.0 and M_w = 9.0. The vertical bars show the uncertainty associated with the standard error of the estimate in $\hat{m}_b$ versus M_w, ± 0.17. (c) The source spectrum of the Pasadena Wood-Anderson record (radial component) of the 1964 Alaska earthquake (M_w = 9.2).

Hartzell and Heaton (1985) obtained source spectra from hand-digitized teleseismic records of 61 large and great earthquakes recorded by the Pasadena, California, Benioff 1-90 seismometer. They found significant differences between spectra of similar size earthquakes. They grouped the earthquakes in five magnitude ranges (M_w = 7.0 to 7.5, 7.5 to 8.0, 8.0 to 8.5, 8.5 to 9.0, and 9.0 to 9.5), averaged together the spectra in each group, and plotted the averages in their Figure 11a. We adjust their spectra (which are heavily smoothed) to be consistent with our choice of parameters (α, ρ, t^*, $R_{\theta\phi}$, C). With the following changes, we average the spectra

of the earthquakes in the same five magnitude ranges and plot the averages in Figure 11a. Using a P-wave velocity, $\alpha = 6.5$ km/sec, as we do, instead of Hartzell and Heaton's (1985) $\alpha = 8.0$ km/sec lowers the level of the spectra. Using a radiation pattern computed separately for each event from the mechanisms in Hartzell and Heaton's (1985) Table 1, as we do, also has the effect, in general, of lowering the level of the spectra, because Hartzell and Heaton (1985) correct each spectrum with the same average P-wave radiation coefficient and ignore the pP and sP phases (the inclusion of which increases the amplitude of the radiation pattern). The spectral shapes have changed because we use $t^* = 0.7$ sec instead of $t^* = 1.0$ sec. We also reclassify the 1957 Aleutian event, their earthquake no. 42, into a lower moment range, $M_w = 8.5$ to 9.0, as suggested by Ruff *et al.* (1985). Because of digitization error, the 1-90 spectra are not reliable at periods shorter than 2 sec. The ω^{-2} model specified in (8) is shown for reference. The only earthquake analyzed by Hartzell and Heaton (1985) and us is the 1983 Akita-Oki event. For that event, our average spectrum from GDSN records agrees well with the spectrum of the Pasadena 1-90 record. Figure 11a and Hartzell and Heaton's Figure 11a show an apparent saturation of spectral amplitude with increasing moment.

Figure 11b shows the average of the six source spectra presented in Figure 7. The average M_w for those six events is 7.63. Therefore, the average spectrum from this study falls below the ω^{-2} model described in (8) by about 0.4 M_w units or, equivalently, 0.6 log M_0 units. However, it lies above Hartzell and Heaton's (1985) average spectrum for $M_w = 7.5$ to 8.0. The average spectrum from this study does not have a spectral structure suggested by Gusev. The spectral amplitudes in (7) estimated from $\hat{m}_b$ are also shown by dots in Figure 11b. They do not show the saturation of spectral amplitude with increasing moment that is seen in the 1-90 spectra (Figure 11a).

The spectrum of the Pasadena, California, Wood-Anderson record of the 1964 Alaskan earthquake is shown in Figure 11c. We estimated vertical displacements from the horizontal Wood-Anderson record (radial component) using Gutenberg's calibration for PH waves. The level of the spectrum is consistent with the ω^{-2} model described in (8) and with the spectral amplitude obtained from $\hat{m}_b$ in the previous section, but it is not consistent with the saturation of spectral amplitude with increasing moment seen in Figure 11a. Since we reclassified the 1957 Aleutian earthquake into a lower magnitude range, our magnitude range 9.0 to 9.5 in Figure 11a contains only two events: the 1960 Chilean earthquake and the 1952 Kamchatka earthquake (which could be moved to a lower magnitude range, too). Hartzell and Heaton (1985) and our studies did not include the 1964 Alaskan earthquake spectrum in the average spectra because the 1-90 record for that event is offscale. Similarly, Hartzell (personal communication, 1985) notes that the Wood-Anderson record of the 1964 Alaskan earthquake is significantly bigger than the Wood-Anderson record of the 1960 Chilean earthquake after correction for the effects of distance. This is consistent with the levels of the spectra shown in Figure 11, a and c. If an onscale 1-90 record was available for the 1964 Alaska earthquake, Hartzell and Heaton's average spectrum for M_w between 9.0 and 9.5 (their Figure 11a) would be significantly higher.

Taken together, the data from this study (Figure 11, b and c) show spectral levels slightly above the 1-90 spectral levels for M_w from 7.0 to 8.5. For M_w from 8.5 to 9.5, our analysis of $\hat{m}_b$ indicates spectral levels significantly higher than the 1-90 levels.

Rather than discuss the differences and similarities between the models, we prefer to emphasize the differences between different events and the importance of

determining the whole spectrum. The ω^{-2} model is a simple and useful reference model for discriminating between different earthquakes. However, the spectra of individual earthquakes deviate from the model considerably.

See Boore (1986) for further discussion of how $\hat{m}_b$ and M_S might discriminate between various spectral models. Boore (1983) develops a stochastic method for simulation of near-field strong ground motions using random vibration theory. He demonstrates that an ω^{-2} model with $\Delta\sigma$ of 100 bars can explain essential aspects of strong ground motions for earthquakes in western North America with M_w of 5.0 to 7.7. Boore (1986) extends this method to simulate teleseismic P waves and finds that an ω^{-2} model with $\Delta\sigma$ of 50 bars explains our $\hat{m}_b$ values for earthquakes with M_w up to 9.5.

Implications for Local Magnitude

Although it is known (Brune, 1970; Kanamori, 1979) that local magnitude, M_L, appears to saturate for California strike-slip events at about $7\frac{1}{4}$, the behavior of M_L is not known for great thrust earthquakes. Since $\hat{m}_b$ and M_L represent the amplitudes of seismic waves at about the same period, the behavior of M_L for great earthquakes may be similar to $\hat{m}_b$. However, the rupture plane-site geometry may be an important factor. Since $\hat{m}_b$ is determined at teleseismic distances, seismic radiation from the entire fault plane contributes to $\hat{m}_b$ equally. In contrast, M_L, which is determined in the near-field, weights the closest part of the fault plane more heavily. Hence, it is possible that M_L for great thrust earthquakes saturates as M_w increases, even though $\hat{m}_b$ does not.

Application to Strong Motion Prediction

In this section, we illustrate how our teleseismic data can constrain strong motion modeling of great earthquakes. Kanamori (1979) simulated the rupture of a one-dimensional strike-slip fault. Here, we extend his approach to a two-dimensional, dipping fault plane. The fault plane is divided into subfaults and empirical Green's functions (or subevents) are superimposed with some randomness. The technique of superposition of Green's functions has been used by many workers and can be implemented in different ways. Our procedure adheres to two principles: (1) it is consistent with gross seismological parameters of the event to be simulated and the subevent, such as total moment, fault dimensions, and presence of large scale asperities, and (2) it incorporates randomness in several different ways.

In our procedure, the displacement at the site can be expressed as

$$d(t) = \sum_{i=1}^{I} \sum_{j=1}^{J} f_{ij}(t - \eta_{ij}) \tag{10}$$

where $f_{ij}(t)$ is the displacement at the site due to the ijth point source, t is time, I and J are the number of subfaults into which the two-dimensional fault plane is divided in length and width, and η_{ij} is the delay applied to the ijth subfault to simulate rupture propagation. To make the procedure physically realistic, we chose I and J so that the length and width of the subfault are equal to the length and width of the subevent rupture. η_{ij} is calculated by dividing the distance from the hypocenter to the ijth subfault by a rupture velocity chosen from a Gaussian distribution. The rupture front is thus roughly circular.

In using this method, we neglect the effects of radiation pattern and dispersion and assume that attenuation and geometrical spreading can be approximated by a

power law decay in amplitude with distance. With these assumptions, $f_{ij}(t)$ can be written

$$f_{ij}(t) = \left[\frac{\Delta_0}{\Delta_{ij}}\right]^p g_{ij}\left(t - \frac{1}{c}\Delta_{ij}\right) \tag{11}$$

where $g_{ij}(t)$ is the displacement at the site due to the ijth subfault at distance Δ_0, the distance at which the subevent record was written, Δ_{ij} is the distance between the ijth subfault and the site, p is the power of the attenuation, and c is the phase velocity (assumed to be 6.0 km/sec for the teleseismic calculation and 3.0 km/sec for the near-field calculation). Δ_{ij} is calculated from the three-dimensional relationship of the dipping fault plane to the site.

It remains to obtain g_{ij} by summing subevent records

$$g_{ij}(t) = m_{ij} \sum_{k=1}^{n_{ij}} g_0(t - \tau_{ijk}) \tag{12}$$

where $g_0(t)$ is the subevent record, τ_{ijk} is a time delay, n_{ij} is determined from the strength of the subfault, and m_{ij} is a factor near 1 chosen so that an integral number of subevent records, n_{ij}, can sum to a desired subfault moment. That is, $n_{ij} = [M_{ij}/m_0]$ and $m_{ij} = M_{ij}/n_{ij}$ where M_{ij} is the moment assigned to each subfault, m_0 is the moment of the subevent, and [ ] means nearest integer to the argument. In our implementation, M_{ij} can be drawn from one of two Gaussian distributions, of which one represents weak zones and the other stronger zones (asperities). We specify the average values and the standard deviations of the Gaussian distributions so that the total moment of the subevents sums to the moment, M_0, of the event to be simulated. That is, $\langle M_{ij}\rangle = M_0/IJ$ where $\langle\ \rangle$ means the average value of the argument. τ_{ijk} in (12) is randomly drawn from a uniform distribution between 0 and $n_{ij}\tau$ where τ is a somewhat arbitrary time; we chose τ to be roughly the effective width of the time function of the subevent. The calculation is not sensitive to τ. As discussed in Kanamori (1979), randomly picking τ_{ijk} is a middle course between the two extremes of summing all the subevent records at once [e.g., $g_{ij}(t) = m_{ij}n_{ij}g_0(t)$] and delaying each subevent record by a uniform time [e.g., $g_{ij}(t) = m_{ij}\sum_{k=1}^{n_{ij}} g_0(t - k\tau)$]. Using the first scheme increases the maximum amplitude of simulated ground motions produced by a long strike-slip rupture by a factor of 4 compared to the second scheme (see Figure 7 of Kanamori, 1979). The middle course of picking τ_{ijk} randomly produces amplitudes half as large as the first and twice as large as the second scheme.

To make this calculation, we must choose an appropriate subevent and a typical subevent record to serve as $g_0(t)$. We chose the 1971 San Fernando earthquake (no. 17 in Table 1; $M_w = 6.6$) because it was a thrust event that was well-recorded in both the near- and far-field. For the San Fernando earthquake, we chose τ to be 2 sec (Langston, 1978). We used the Matsushiro, Japan, short-period WWSSN record ($\Delta_0 = 80°$) as $g_0(t)$. We simulated five great subduction earthquakes (1960 Chile, 1964 Alaska, 1965 Rat Island, 1963 Kurile Island, and 1968 Tokachi-Oki) using the summation procedure outlined above. The dip of the fault plane was assumed to be 30°. We chose a rupture velocity of 2.5 km/sec with a standard deviation of 0.3 km/sec. Attenuation was not included in the teleseismic simulations [e.g., $\Delta_{ij} \approx \Delta_0$ or, equivalently, $p = 0$ in (11)]. Therefore, the simulated WWSSN records must be considered to be at the same distance as $g_0(t)$. Examples of the observed and simulated traces are shown in Figure 12. For each earthquake, an average $\hat{m}_b$ is

calculated from five or more simulations with different random seeds. The resulting simulated $\hat{m}_b$'s are shown as black squares in Figure 2. The simulated $\hat{m}_b$'s are about 0.3 $\hat{m}_b$ units larger than the observed $\hat{m}_b$'s (except for the 1960 Chilean earthquake). Considering that the difference in moment between the subevent and the event to be simulated is three to four orders of magnitude, the agreement between the observed and the simulated $\hat{m}_b$'s is good. The entire fault plane was assumed to have uniform strength in the teleseismic simulations. Including large-scale asperities increased the displacement amplitudes only about 20 per cent (Houston and Kanamori, 1984a, b).

This simulation procedure can be applied to predict the amplitude and duration

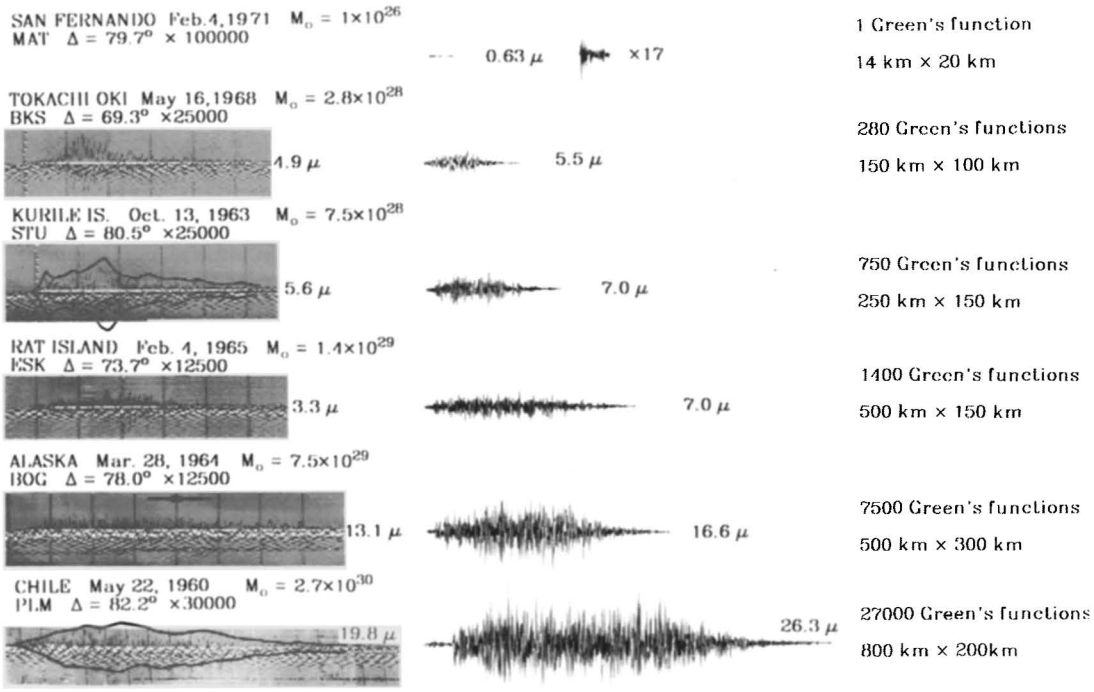

FIG. 12. A comparison between actual records and the simulated records for five great earthquakes. Length and width of the fault plane and the number of subevent records summed are given on the *right*. Minute marks are visible on the WWSSN and Benioff records. Distances and gains are given for the WWSSN and Benioff records. The amplitude of the ground motion in microns is shown next to each trace. The record from WWSSN station MAT of the 1971 San Fernando earthquake has been digitized and serves as the subevent record. It is shown both to scale and expanded 17 times for ease of viewing. All simulated traces represent teleseismic records at a distance of 80°, which is the distance from San Fernando to the station MAT. Note the overall similarity of character between the simulated and actual records.

of strong ground motion given the rupture plane and moment of an earthquake by choosing for $g_0(t)$ a near-field strong motion record. Coats *et al.* (1984) used the method described above to simulate the near-field motions at Anchorage, Alaska, caused by the 1964 Alaska earthquake. As various $g_0(t)$'s, Coats *et al.* used three 1971 San Fernando strong motion records written at distances of 40 to 110 km: H121; N191; and O206 (Hudson *et al.*, 1969). The dip of the fault plane was prescribed to be 15°. The calculations assumed an average rupture velocity of 3.0 km/sec with a standard deviation of 0.3 km/sec. They included the large asperity determined from deconvolutions of long-period body waves (Ruff and Kanamori, 1982); subfaults within the asperity were assumed to release about twice as much moment as subfaults in the weak zone. Using uniform moment release decreased

the velocities at the site by a factor of about 1.3 over those produced by the fault plane containing the asperity. This factor would increase if the asperity were assumed to be stronger. Both amplitude and duration of the strong motion were somewhat sensitive to the degree of attenuation that was assumed. The power, p, in (11) was prescribed to be 1.7. Coats *et al.* computed M_L's of 7.4 to 7.8 and peak-to-peak displacements at the site averaging 35 cm. The duration of significant motion exceeded 3 min. It is not clear whether the M_L's should be adjusted downward by the amount that the simulated $\hat{m}_b$ for 1964 Alaska is too high. Ultimately, small earthquakes from a given seismogenic zone recorded at the site under consideration can be used as subevents, thus reducing the considerable uncertainty caused by propagation and site effects.

The success of a summation scheme depends on the way in which the subevent records are superposed (e.g., the number of subevent records and their relative timing). This can be understood in the frequency domain as a requirement that the summation procedure take the spectrum of the subevent to an appropriate spectrum for the earthquake to be simulated. The discrepancy between the actual and simulated $\hat{m}_b$ seen in Figure 2 could be due to the choice of a very impulsive, high stress drop earthquake to serve as the subevent. In an essentially similar approach, strong motions can be modeled in the frequency domain directly (e.g., Boore, 1983) if the source spectrum of the event to be simulated can be assumed. Such modeling should be consistent with the teleseismic data presented in this paper.

Conclusions

A new teleseismic body-wave magnitude, $\hat{m}_b$, is defined using the maximum amplitude achieved by the P-wave train rather than the amplitude in the first few cycles of the P wave. Analysis of WWSSN short-period teleseismic records of 19 large to great earthquakes shows that $\hat{m}_b$ does not saturate with increasing M_w. The empirical relation between $\hat{m}_b$ and M_w is given by (2). We chose to further parameterize the complex short-period waveform by the coda length and the build-up time to the maximum amplitude. These data are consistent witha simple model of rupture propagating at a velocity of 2.5 km/sec across a fault plane with asperities. Figure 4b confirms that short-period waves are generated preferentially in the same regions of the fault plane as longer period waves with periods of 10 to 50 sec, and to some extent supports the mapping of moment release on the fault plane performed by other workers by deconvolutions of long-period waves.

Magnitude scales are, by definition, a measurement at one period only and may give an inadequate and sometimes incorrect indication of the source spectrum. The moment rate spectra that we determined directly from intermediate-period and short-period teleseismic digital records are shown in Figures 7 and 8. Significant differences in spectral fall-off occur between events, and may be due to differences in seismic coupling.

Using the short-period digital records, we obtain an empirical relation between time-domain amplitude and spectral amplitude for short-period waves. Spectral amplitudes are estimated from the $\hat{m}_b$ data. We compare our results to the ω^{-2} and Gusev spectral models in Figures 10 and 11b. Neither model can completely represent the data. Nevertheless, we consider the ω^{-2} model a useful reference model for comparing different events. The average source spectrum of the six large events analyzed here does not have a spectral structure suggested by Gusev.

An application to strong motion modeling is presented in which a 1971 San Fernando teleseismic short-period record is summed up to simulate teleseismic records produced by five great earthquakes. The summation procedure matches the

moment of the event to be simulated and includes rupture propagation, fault plane roughness, and randomness. The $\hat{m}_b$ data constrains the summation procedure at periods of 1 to 2 sec. The simulated $\hat{m}_b$'s are about 0.3 $\hat{m}_b$ units larger than the observed $\hat{m}_b$'s (except for the 1960 Chilean earthquake). Considering that the difference in moment between the subevent and the event to be simulated is three to four orders of magnitude, the agreement between the observed and the simulated $\hat{m}_b$'s is good. This method can also be evaluated in the frequency domain using the source spectra that we have determined from digital records. Thus constrained at short periods by teleseismic data, this summation procedure can be more confidently used with near-field strong motion records as Green's functions to predict strong motions from great earthquakes.

ACKNOWLEDGMENTS

We thank Dave Boore for encouragement and helpful discussions and a review of an early version of this paper. We also had helpful discussions with Doug Coats. Steve Hartzell made the Pasadena Benioff 1-90 records and spectra readily available. Inez Cifuentes sent us copies of short-period records of the 1960 Chilean earthquake. Jia-Jun Zhang helped us to read SRO tapes written before 1980. C. Langston provided digitized teleseismic records of the 1971 San Fernando earthquake. M. Kikuchi provided the results of his deconvolutions of moment release. Allen Olson, Art Frankel, and John Vidale reviewed the manuscript. This research was supported by Exxon Production Research, Agreement PR-7373 and U.S. Geological Survey Grant 14-08-0001-G-979.

REFERENCES

Aki, K. (1967). Scaling law of seismic spectrum, *J. Geophys. Res.* **73,** 1217–1231.

Aki, K. (1972). Scaling law of earthquake source time-function, *Geophys. J. R. Astr. Soc.* **31,** 3–25.

Aki, K. (1983). Strong-motion seismology, *Proceedings of the International School of Physics, Enrico Fermi, Earthquakes Observation, Theory and Interpretation,* H. Kanamori and E. Boschi, Editors.

Beck, S. and L. Ruff (1984). The rupture process of the great 1979 Colombia earthquake: evidence for the asperity model, *J. Geophys. Res.* **89,** 9281–9291.

Beck, S. and L. Ruff (1985). The rupture process of the 1976 Mindanao earthquake, *J. Geophys. Res.* **90,** 6773–6782.

Boore, D. M. (1983). Stochastic simulation of high-frequency ground motions based on seismological models of the radiated spectra, *Bull. Seism. Soc. Am.* **54,** 1865–1894.

Boore, D. (1986). Short-period *P*- and *S*-wave radiation from large earthquakes: implications for spectral scaling relations, *Bull. Seism. Soc. Am.* **76,** 43–64.

Boore, D. M. and J. Boatwright (1984). Average body-wave radiation coefficients, *Bull. Seism. Soc. Am.* **74,** 1615–1621.

Brune, J. (1970). Tectonic stress and the spectra of seismic shear waves from earthquakes, *J. Geophys. Res.* **75,** 4997–5009.

Butler, R., G. S. Stewart, and H. Kanamori (1979). The July 27, 1976 Tangshan, China earthquake—A complex sequence of intraplate events, *Bull. Seism. Soc. Am.* **69,** 207–220.

Chael, E. and G. Stewart (1982). Recent large earthquakes along the Middle American Trench and their implications for the subduction process, *J. Geophys. Res.* **87,** 329–338.

Coats, D., H. Kanamori, and H. Houston (1984). Simulation of the strong motion from the 1964 Alaskan earthquake (abstract), *Earthquake Notes* **55,** 18.

Der, Z. A. and A. C. Lees (1985). Methodologies of estimating $t^*(f)$ from short-period body waves and regional variations of $t^*(f)$ in the United States, *Geophys. J. R. Astr. Soc.* (in press).

Eissler, H. K. and H. Kanamori (1985). Depth estimates of large earthquakes on the island of Hawaii since 1940, *J. Geophys. Res.* (in press).

Gusev, A. A. (1983). Descriptive statistical model of earthquake source radiation and its application to an estimation of short-period strong motion, *Geophys. J. R. Astr. Soc.* **74,** 787–808.

Hartzell, S. H. and T. H. Heaton (1983). Inverison of strong ground motion and teleseismic waveform data for the fault rupture history of the 1979 Imperial Valley, California, earthquake, *Bull Seism. Soc. Am.* **73,** 1553–1583.

Hartzell, S. H. and T. H. Heaton (1985). Teleseismic time functions for large shallow subduction zone earthquakes, *Bull. Seism. Soc. Am.* **75,** 965–1004.

Haskell, N. (1964). Total energy and energy spectral density of elastic wave radiation from propagating faults, *Bull. Seism. Soc. Am.* **54,** 1811–1842.

Haskell, N. (1966). Total energy and energy spectral density of elastic wave radiation from propagation faults, 2, *Bull. Seism. Soc. Am.* **56,** 125–140.

Houston, H. and H. Kanamori (1983). Rupture process of great earthquakes at short periods (abstract), *EOS, Trans. Am. Geophys. Union* **64,** 771.

Houston, H. and H. Kanamori (1984a). The effect of asperities on short-period seismic radiation with application to the 1964 Alaskan earthquake (abstract), *Earthquake Notes* **55,** 18.

Houston, H. and H. Kanamori (1984b). Source spectra of great earthquakes at high frequencies (abstract), *EOS Trans. Am. Geophys. Union* **65,** 990.

Hudson, D. E., M. D. Trifunac, and A. G. Brady (1976). Analysis of strong motion accelerograms, Index vol. (EERL Report No. 76-02), Earthquake Engineering Research Laboratory, California Institute of Technology, Pasadena, California.

Kanamori, H. (1967). Attenuation of *P* waves in the upper and lower mantle, *Bull. Earthquake Res. Inst., Tokyo Univ.* **45,** 299–312.

Kanamori, H. (1979). A semi-empirical approach to prediction of long period ground motions from great earthquakes, *Bull. Seism. Soc. Am.* **69,** 1645–1670.

Kanamori, H. and G. Stewart (1976). Mode of the strain release along the Gibbs fracture zone, Mid-Atlantic Ridge, *Phys. Earth Planet. Interiors* **11,** 312–332.

Kanamori, H. and G. Stewart (1978). Seismological aspects of the Guatemala earthquake of February 4, 1976, *J. Geophys. Res.* **83,** 3427–3434.

Kikuchi, M. and H. Kanamori (1982). Inversion of complex body waves, *Bull. Seism. Soc. Am.* **72,** 491–506.

Koyama, J. and S. Zheng (1983). Excitation of short-period body waves by recent great earthquakes, ZISIN, *J. Seis. Soc. Japan* **36,** 237–245. (in Japanese with English abstract).

Koyama, J. and S. Zheng (1985). Excitation of short-period body waves by recent great earthquakes, *Phys. Earth Planet. Interiors* **37,** 108–123.

Langston, C. A. (1978). The February 9, 1971 San Fernando earthquake: a study of source finiteness in teleseismic body waves, *Bull. Seism. Soc. Am.* **68,** 1–29.

Lay, T., H. Kanamori, and L. Ruff (1982). The asperity model and the nature of large subduction zone earthquakes, *Earthquake Prediction Res.* **1,** 3–71.

Purcaru, G. (1984). Rupture process pattern of earthquakes from frequency-time-dependent body-wave magnitudes $m_B(t, T)$ and a subasperity model (abstract), IASPEI, Regional Meeting, abstract volume, Hyderabad, India, October 31–November 7, 19, 1984.

Ruff, L. and H. Kanamori (1980). Seismicity and the subduction process, *Phys. Earth Planet. Interiors* **23,** 240–252.

Ruff, L. and H. Kanamori (1983). The rupture process and asperity distribution of three great earthquakes from long-period diffracted *P*-waves, *Phys. Earth Planet. Interiors* **31,** 202–330.

Ruff, L., H. Kanamori, and L. Sykes (1985). The 1957 great Aleutian earthquake (abstract), *EOS, Trans. Am. Geophys. Union* **66,** 298.

Stewart, G. and S. N. Cohn (1979). The 1976 August 16, Mindanao Phillipine earthquake (M_S = 7.8)—Evidence for a subduction zone south of Mindanao, *Geophys. J. R. Astr. Soc.* **57,** 51–65.

Stewart, G. S. and H. Kanamori (1982). Complexity of rupture in large strike-slip earthquakes in Turkey, *Phys. Earth Planet. Interiors* **28,** 70–84.

SEISMOLOGICAL LABORATORY AND
DIVISION OF GEOLOGICAL AND PLANETARY SCIENCES
CALIFORNIA INSTITUTE OF TECHNOLOGY
PASADENA, CALIFORNIA 91125
CONTRIBUTION NO. 4228

Manuscript received 29 May 1985